Mathematical Biosciences and Engineering

MBE, 19(9): 9437–9456.
DOI: 10.3934/mbe.2022439
Received: 20 April 2022
Revised: 15 June 2022
Accepted: 20 June 2022
Published: 28 June 2022

http://www.aimspress.com/journal/MBE

Research article

Intermuscular coupling network analysis of upper limbs based on R-vine copula transfer entropy

Shaojun Zhu[1], Jinhui Zhao[2,*], Yating Wu[3] and Qingshan She[3,*]

[1] Hangzhou Xinyizhen Technology Company Limited, Hangzhou 310018, China
[2] College of Electrical Engineering, Zhejiang University of Water Resources and Electric Power, Hangzhou 310018, China
[3] College of Automation, Hangzhou Dianzi University, Hangzhou 310018, China

* **Correspondence:** Email: jhzhao2009@ zju.edu.cn, qsshe@hdu.edu.cn.

Abstract: In the field of neuroscience, it is very important to evaluate the causal coupling characteristics between bioelectrical signals accurately and effectively. Transfer entropy is commonly used to analyze complex data, especially the causal relationship between data with non-linear, multidimensional characteristics. However, traditional transfer entropy needs to estimate the probability density function of the variable, which is computationally complex and unstable. In this paper, a new and effective method for entropy transfer is proposed, by means of applying R-vine copula function estimation. The effectiveness of R-vine copula transfer entropy is first verified on several simulations, and then applied to intermuscular coupling analysis to explore the characteristics of the intermuscular coupling network of muscles in non-fatigue and fatigue conditions. The experiment results show that as the muscle group enters the fatigue state, the community structure can be adjusted and the muscle nodes participating in the exercise are fully activated, enabling the two-way interaction between different communities. Finally, it comes to the conclusion that the proposed method can make accurate inferences about complex causal coupling. Moreover, the characteristics of the intermuscular coupling network in both non-fatigue and fatigue states can provide a new theoretical perspective for the diagnosis of neuromuscular fatigue and sports rehabilitation, which has good application value.

Keywords: R-vine copula; transfer entropy; surface EMG; muscle fatigue

1. Introduction

Electroencephalography (EEG) and electromyogram (EMG) signals can reflect motor control information and functional response information, hence multi-temporal and spatial-level cortical-muscle coupling has become a hot research topic in motor neuroscience [1,2]. The concept of intermuscular coupling (IMC) is derived from cortical muscle coupling, which refers to the interaction and interconnection between related muscles under a specific movement task [3]. This particular coupling relationship quantifies the corticospinal drive that is shared among motor neurons. It has been reported that the muscular coupling has significant frequency difference, which manifests the different innervation modes and regulation strategies of the nervous system to muscle contraction [4]. At present, the research on intermuscular coupling is mainly concentrated in the fields of sports medicine and rehabilitation engineering [5,6].

Surface electromyogram (sEMG) signal is a more objective, accurate and non-invasive physiological feedback signal in the current study of muscle fatigue state recognition [7]. It depends on several physiological parameters of muscles, such as discharge frequency, conduction velocity, the number and type of motor units, muscle fibers, recruitment mode, and a low-pass filter effect conductor [8]. Murillo-Escobar et al. [9] analyzed muscle fatigue during dynamic contractions by fusing time and spectral domain features, permutation entropy and biomechanical features. Edward et al. [10] proposed a new framework based on Fourier descriptor-based shape representation and geometric feature extraction, using the geometric features of sEMG signals to distinguish between non-fatigue and fatigue states of muscles. Additionally, in the field of human-robot interaction [11,12], sEMG signals have been also widely used and yielded amazing results [13–17].

In recent years, complex network theory has attracted significant attention from a large number of researchers, especially in the field of brain function networks [18]. Complex network analysis aims to abstract the internal units of the system as network nodes and the relationships between the units are connected in the form of edges. Through the properties of network topology, the evolution rules and dynamic behavior of the complex system can be understood. Kerkman et al. [19] combined coherence and non-negative matrix factorization algorithms to analyze the sEMG signals obtained from 36 bilateral muscles of the whole body and the connectivity network analysis between all muscle pairs showed that the modularity of the neuromuscular system combines anatomically and functionally connected muscles. It also indicates that the intermuscular coupling network provides a unique window for clarifying the motor control mechanism [20]. There are few studies on the direction of information transmission in the intermuscular coupling network.

The Granger causality (GC) analysis method based on the multivariate autoregressive model is relatively simple in calculation and can effectively describe the two-way connection in the network. However, it ignores the correlation items of the model coefficients and can only measure the linear causality among time series [21,22]. The Shannon transfer entropy (STE) proposed by Schreiber [23], as an asymmetric extension of mutual information (MI), contains the causal direction and dynamic strength, with model-free, nonlinear and quantitative analysis. It has been widely used to explore the characteristics of nonlinear causal coupling among neurophysiological signals. However, when available data is limited and the expected entropy is rather small, STE is prone to serious miscalculations. Marschinski et al. [24] proposed an effective transfer entropy (ETE) improvement method, which explicitly considers the limited sample effect and corrects the deviation by setting a significance threshold. However, traditional transfer entropy that depends on the transition probability

needs to accurately estimate the joint probability density function of the variables, which is very sensitive to dimensional changes and computation complexity is high and unstable [25].

The Sklar theorem in statistics states that a joint distribution function is determined by a corresponding copula function [26]. As a link between joint distribution and marginal distribution, the copula function describes all the correlations between variables. In practical applications, they need to be well matched with the distribution type of data. When the dimensionality of the variable increases, the estimated parameters of the typical binary Copula function will increase rapidly, and the "curse of dimensionality" problem will appear [27]. Recently, the development of regular vine (R-vine) copula is based on the idea of a paired copula, assuming conditional independence between specific elements in the distribution to avoid the aforementioned parameter restrictions and other problems [28]. The copula function has been used to estimate causality [29].

In order to solve the problem of accurately estimating the joint probability distribution between variables in the calculation process of traditional transfer entropy method, this paper uses the copula function to calculate the transfer entropy value. Moreover, considering that single copula function has single form, wherein the model fitting is easily distorted and cannot accurately describe the functional coupling characteristics between all bioelectrical signals, the R-vine copula function is introduced and a new method of R-vine copula multivariable transfer entropy (RVCMTE) is proposed in this paper. According to the copula entropy equivalence principle [30], the transfer entropy is extended to high-dimensional cases, inheriting many advantages of R-vine copula. First, the steps of the proposed method are briefly introduced. Second, the effectiveness of the proposed method is verified on numerous simulation examples. Finally, to further explore the intermuscular coupling characteristics under fatigue, the intermuscular coupling network in the state of non-fatigue and fatigue is established on the basis of the proposed method and the knowledge of graph theory is used to discuss the difference in the intermuscular coupling characteristics. This can provide a new theoretical basis for exploring the diagnosis and rehabilitation of neuromuscular diseases.

2. Materials and methods

2.1. R-vine copula

A typical R-vine consists of a tree, node, and an edge. There are several nodes on each level of the tree and each node represents a variable or conditional variable. The connection between two nodes is called an edge and each edge represents the paired copula (pair-copula) of two adjacent nodes [31]. An R-vine structure diagram represents the decomposition form of a multi-dimensional copula density function. Specifically, the R-vine structure of N-channel sEMG signals is composed of $N-1$ layers of trees $T_1, T_2, \ldots, T_{N-1}$, where the node set of the *i*-th tree is denoted as N_t and the edge set is denoted as E_i, $i = 1, 2, ..., N-1$. They meet the following conditions:

1) The node set $N_1 = \{1, 2, ..., N\}$ of tree T_1, the edge set is E_1;

2) For $i = 1, 2, \ldots, N-1$, T_i is a tree with nodes $N_i = E_i$ and edge set E_i;

3) If two edges in tree T_i are connected by edges in tree T_{i+1}, then the two edges must have a common node in the tree T_i.

Next, an N-dimensional R-vine statistical model is built. Suppose the random vector formed by the N-channel sEMG signal $x_1, x_2, ..., x_N$ is $X = \{x_1, x_2, ..., x_N\}$, where the edge density function of the

i-th variable x_i is f_i, $i=1,2,...,N$, then the joint probability density function of X can be expressed as

$$f(x_1,x_2,...,x_N)=[\prod_{i=1}^{N-1}\prod_{e\in E_i}c_{j(e),k(e)|D(e)}(F(x_{j(e)}\mid x_{D(e)}),F(x_{k(e)}\mid x_{D(e)}))]\times[\prod_{i=1}^{N}f_i(x_i)] \tag{1}$$

where $e=j(e),k(e)\mid D(e)$, $j(e)$ and $k(e)$ in E_i are the two nodes connected to the edge e, $D(e)$ is the condition set, $c_{j(e),k(e)|D(e)}$ is the pair-copula density function corresponding to edge e, and conditional distributions $F(x_{j(e)}\mid x_{D(e)})$ and $F(x_{k(e)}\mid x_{D(e)})$ called transformed variables, connect $x_{j(e)}$ with $x_{k(e)}$ given the variables $D(e)$.

On the basis of directional graphs, Dissmann et al. [32] proposed the concept of the R-vine matrix, which allows us to calculate the R-vine copula more conveniently. Since the R-vine matrix is not uniquely determined, for a given N-dimensional R-vine, there are 2^{N-1} different R-vines. To determine the most appropriate R-vine structure model, the maximum spanning tree (MST) algorithm is used in our paper. The key to the MST algorithm is to ensure that the sum of the absolute values of Kendall's τ of each tree node on the R-vine structure is maximized. The Akaike Information Criterion (AIC) is used to select the optimal pair-copula function from a set of copula functions. The calculation formula of AIC is given as

$$\mathrm{AIC}=-2\ln(L)+2k \tag{2}$$

where k is the number of parameters in the pair-copula function, and L is the maximum likelihood value of the pair-copula function. The smaller the AIC value, the better the fit of the R-vine model. After determining the optimal pair-copula function, the maximum likelihood estimation method is further used to estimate the parameters in each pair-copula function.

2.2. R-vine copula transfer entropy

According to Schreiber [23], for two time series $\mathbf{x}$ and $\mathbf{y}$ that satisfy Markov chain properties, the transfer entropy from $\mathbf{x}$ to $\mathbf{y}$ is defined in the form of entropy as follows:

$$\mathrm{TE}_{\mathbf{x}\to\mathbf{y}}=H(x_{i-\tau}^{(k)},y_{i-t}^{(l)})+H(y_i,y_{i-t}^{(l)})-H(x_{i-\tau}^{(k)},y_i,y_{i-t}^{(l)})-H(y_{i-t}^{(l)}) \tag{3}$$

where $H(\cdot)$ represents the Shannon entropy between variables, k and l represent embedding dimensions, and τ and t represent lag time. For two sets of time series $\mathbf{X}=(\mathbf{x}_1,\mathbf{x}_2,...,\mathbf{x}_m)$ and $\mathbf{Y}=(\mathbf{y}_1,\mathbf{y}_2,...,\mathbf{y}_n)$, Eq (3) can be used to compute the multivariate transfer entropy (MTE) from $\mathbf{X}$ to $\mathbf{Y}$ as follows:

$$\begin{aligned}\mathrm{MTE}_{\mathbf{X}\to\mathbf{Y}}=&H(x_{1,i-\tau_1}^{(k_1)},x_{2,i-\tau_2}^{(k_2)},...,x_{m,i-\tau_m}^{(k_m)},y_{1,i-t_1}^{(l_1)},y_{2,i-t_2}^{(l_2)},...,y_{n,i-t_n}^{(l_n)})+\\&H(y_{1,i},y_{2,i},...,y_{n,i},y_{1,i-t_1}^{(l_1)},y_{2,i-t_2}^{(l_2)},...,y_{n,i-t_n}^{(l_n)})-\\&H(x_{1,i-\tau_1}^{(k_1)},x_{2,i-\tau_2}^{(k_2)},...,x_{m,i-\tau_m}^{(k_m)},y_{1,i},y_{2,i},...,y_{n,i},y_{1,i-t_1}^{(l_1)},y_{2,i-t_2}^{(l_2)},...,y_{n,i-t_n}^{(l_n)})-\\&H(y_{1,i-t_1}^{(l_1)},y_{2,i-t_2}^{(l_2)},...,y_{n,i-t_n}^{(l_n)})\end{aligned} \tag{4}$$

Equation (4) calculates the causal relationship between multiple variables. However, as dimensionality increases, the calculation of entropy suffers from the high complexity of the estimation of the kernel function in the joint probability density. To address this problem, Ma et al. [33] pointed out that multivariate joint entropy can be decomposed into two parts, i.e., edge entropy and a copula entropy.

$$H(x_1, x_2, ..., x_d) = H_c(F(x_1), F(x_2), ..., F(x_d)) + \sum_{i=1}^{d} H(x_i) \tag{5}$$

where d represents the number of variables, $F(\cdot)$ represents the marginal distribution function, and $\mathrm{H}_c(\cdot)$ represents the copula entropy. Copula entropy can be estimated by the Monte Carlo method [32]. Equation (5) lays the foundation for establishing the connection between transfer entropy and the copula function. Substituting Eq (3) into Eq (1) and eliminating the edge entropy at the same time, the copula transfer entropy can be obtained as follows:

$$\mathrm{CTE}_{\mathbf{x}\to\mathbf{y}} = H_c[F(x_{i-\tau}^{(k)}), F(y_{i-t}^{(l)})] + H_c[F(y_i), F(y_{i-t}^{(l)})] - H_c[F(x_{i-\tau}^{(k)}), F(y_i), F(y_{i-t}^{(l)})] - H_c[F(y_{i-t}^{(l)})] \tag{6}$$

In the same way, by substituting Eq (3) into Eq (2), the multivariable transfer entropy of the copula can be rewritten as:

$$\begin{aligned}
\mathrm{CMTE}_{\mathbf{X}\to\mathbf{Y}} =& H_c[F(x_{1,i-\tau_1}^{(k_1)}), F(x_{2,i-\tau_2}^{(k_2)}), ..., F(x_{m,i-\tau_m}^{(k_m)}), F(y_{1,i-t_1}^{(l_1)}), F(y_{2,i-t_2}^{(l_2)}), ..., F(y_{n,i-t_n}^{(l_n)})] + \\
& H_c[F(y_{1,i}), F(y_{2,i}), ..., F(y_{n,i}), F(y_{1,i-t_1}^{(l_1)}), F(y_{2,i-t_2}^{(l_2)}), ..., F(y_{n,i-t_n}^{(l_n)})] - \\
& H_c[F(x_{1,i-\tau_1}^{(k_1)}), F(x_{2,i-\tau_2}^{(k_2)}), ..., F(x_{m,i-\tau_m}^{(k_m)}), \\
& \quad F(y_{1,i}), F(y_{2,i}), ..., F(y_{n,i}), \\
& \quad F(y_{1,i-t_1}^{(l_1)}), F(y_{2,i-t_2}^{(l_2)}), ..., F(y_{n,i-t_n}^{(l_n)})] - \\
& H_c[F(y_{1,i-t_1}^{(l_1)}), F(y_{2,i-t_2}^{(l_2)}), ..., F(y_{n,i-t_n}^{(l_n)})]
\end{aligned} \tag{7}$$

Equation (7) shows that the key to the calculation of copula multivariate transfer entropy lies in each item of the copula entropy, and the calculation of the copula entropy is inseparable from the selected copula function type. In high-dimensional situations, the R-vine copula graphical model proposed by Bedford and Cooke et al. [34] is more flexible than the traditional single-form copula function and can solve problems such as low model accuracy and the curse of dimensionality. Therefore, RVCMTE can be expressed as follows:

$$\begin{aligned}
\mathrm{RVCMTE}_{\mathbf{X}\to\mathbf{Y}} =& H_{c_{R\text{-}Vine}}[F(x_{1,i-\tau_1}^{(k_1)}), F(x_{2,i-\tau_2}^{(k_2)}), ..., F(x_{m,i-\tau_m}^{(k_m)}), F(y_{1,i-t_1}^{(l_1)}), F(y_{2,i-t_2}^{(l_2)}), ..., F(y_{n,i-t_n}^{(l_n)})] + \\
& H_{c_{R\text{-}Vine}}[F(y_{1,i}), F(y_{2,i}), ..., F(y_{n,i}), F(y_{1,i-t_1}^{(l_1)}), F(y_{2,i-t_2}^{(l_2)}), ..., F(y_{n,i-t_n}^{(l_n)})] - \\
& H_{c_{R\text{-}Vine}}[F(x_{1,i-\tau_1}^{(k_1)}), F(x_{2,i-\tau_2}^{(k_2)}), ..., F(x_{m,i-\tau_m}^{(k_m)}), \\
& \quad F(y_{1,i}), F(y_{2,i}), ..., F(y_{n,i}), \\
& \quad F(y_{1,i-t_1}^{(l_1)}), F(y_{2,i-t_2}^{(l_2)}), ..., F(y_{n,i-t_n}^{(l_n)})] - \\
& H_{c_{R\text{-}Vine}}[F(y_{1,i-t_1}^{(l_1)}), F(y_{2,i-t_2}^{(l_2)}), ..., F(y_{n,i-t_n}^{(l_n)})]
\end{aligned} \tag{8}$$

Here, the last term of Eq (8) can be omitted when $\mathbf{y} = y_1$. In other words, $H_{c_{R\text{-}Vine}}[F(y_{1,i-t_1}^{(l_1)})] = 0$.

3. Results

3.1. Simulations

In this section, we describe six model simulations which manifest different causal relationships and compare these against the other methods, including STE and ETE. These six models manifest different causal relationships, including no causality (Model I), linear causality (Model II), nonlinear causality (Model III), the combination of quadratic and exponent (Model IV), causality-in-variance (Model V), and quadratic sine combination model (Model VI). In Model VI, a single Gaussian copula estimated multivariate transfer entropy (GCMTE) is utilized for comparison. To reflect that RVCMTE can estimate the causal characteristics among multiple variables, three variables were selected for the experiment. The respective number of lags defaults to a value of 1.

1) Model I. Starting with a simple model, three random variables x_t, z_t and y_t are completely unrelated as follows

$$\begin{cases} x_t = \varepsilon_{x,t} \\ z_t = \varepsilon_{z,t} \\ y_t = \varepsilon_{y,t} \end{cases} \tag{9}$$

where $(\varepsilon_{x,t}, \varepsilon_{z,t}, \varepsilon_{y,t}) \sim N(0, \Sigma)$, and $\Sigma = \begin{bmatrix} 1 & 0 \\ 0 & 1 \end{bmatrix}$, $t = 2500$. We simulate 2500 observations of these processes.

2) Model II. The random variable y_t has a linear relationship with x_t and z_t. y_t depends on the past of x_t and z_t. On the contrary, x_t and z_t have nothing to do with y_t.

$$\begin{cases} x_t = 0.2x_{t-1} + \varepsilon_{x,t} \\ z_t = 0.5z_{t-1} + \varepsilon_{z,t} \\ y_t = x_{t-1} + z_{t-1} + \varepsilon_{y,t} \end{cases} \tag{10}$$

3) Model III: The random variable y_t has a non-linear relationship with x_t and z_t. y_t depends on the past of x_t and z_t.

$$\begin{cases} x_t = 0.2x_{t-1} + \varepsilon_{x,t} \\ z_t = 0.5z_{t-1} + \varepsilon_{z,t} \\ y_t = \sqrt{|x_{t-1}|} + \sqrt{|z_{t-1}|} + \varepsilon_{y,t} \end{cases} \tag{11}$$

To prevent experimental error caused by unstable data in the previous period, the first 100 observations were discarded as a burn-in period.

4) Model IV: The random variable y_t has a quadratic and exponential relationship with x_t and z_t. y_t depends on the past of x_t and z_t.

$$\begin{cases} x_t = 0.2x_{t-1} + \varepsilon_{x,t} \\ z_t = 0.5z_{t-1} + \varepsilon_{z,t} \\ y_t = \exp(-(x_{t-1}^2 + z_{t-1}^2)/2) + \varepsilon_{y,t} \end{cases} \tag{12}$$

5) Model V： The random variable y_t has a second moment relationship with x_t and z_t. y_t depends on the past of x_t and z_t.

$$\begin{cases} x_t = 0.2x_{t-1} + \varepsilon_{x,t} \\ z_t = 0.5z_{t-1} + \varepsilon_{z,t} \\ y_t = \sqrt{x_{t-1}^2 + z_{t-1}^2} * \varepsilon_{y,t} \end{cases} \tag{13}$$

6) Model VI： The random variable y_t has complicated non-linear, quadratic, and sine-cosine relations with x_t and z_t. y_t depends on the past of x_t and z_t.

$$\begin{cases} x_t = 0.4x_{t-1} + \varepsilon_{x,t} \\ z_t = 0.4y_{t-1} + \varepsilon_{z,t} \\ y_t = (1 + a/10) * [x_{t-1} + \cos^2(z_{t-1})] + \varepsilon_{y,t} \end{cases} \tag{14}$$

Of these, a is the coupling strength and the variation range is [1, 10], which is incremented by 1.

The execution process of the simulation structure is described as follows:

1) Generate data samples of a certain length according to Models I–VI, and the noise factor is 1 by default;

2) Bring the data samples into Eq (8) to obtain the transfer entropy between the variables;

3) Circulate the above process, and then calculate the mean and standard deviation, and perform a significant t-test on the results.

Each of the above models is run 10 times randomly and the corresponding results are shown in Figures 1 and 2. It can be seen from Figure 1(a) that each method delivers very low entropy estimates. There is no causal relationship between *x*, *z*, and *y*, which is consistent with our model settings. It can be seen from Figure 1(b)–(e) that the comparison methods and our algorithm correctly detected the linear, simple nonlinear, complex nonlinear and higher-order moment causality between *x* and *y* and *z* and *y*. RVCMTE gives a better causal comparison effect. In addition, RVCMTE can also correctly detect causal relationships between multiple variables. The value of RVCMTE {*x*, *z*} to *y* is higher than the other values, which matches the model. It can be seen from Figure 2 that compared to Gaussian copula, the R-vine copula is more accurate in characterizing the changes in the causal coupling strength between multiple variables, especially in the target to source direction, RVCMTE≈0, and it remains almost unchanged. The GCMTE value is negative, which is incorrect. The transfer entropy should take the minimum value of 0 when the source variable has no effect on the target variable. In addition, the independent sample t-test is used for the significance test between groups and the significance level is taken as 0.05. The P-values of information flow in the opposite direction are all less than 0.05, which shows a significant difference in the opposite direction. This shows that RVCMTE is more effective in identifying causality and has the function of multivariate causality measurement. RVCMTE further

expands the application scope of TE.

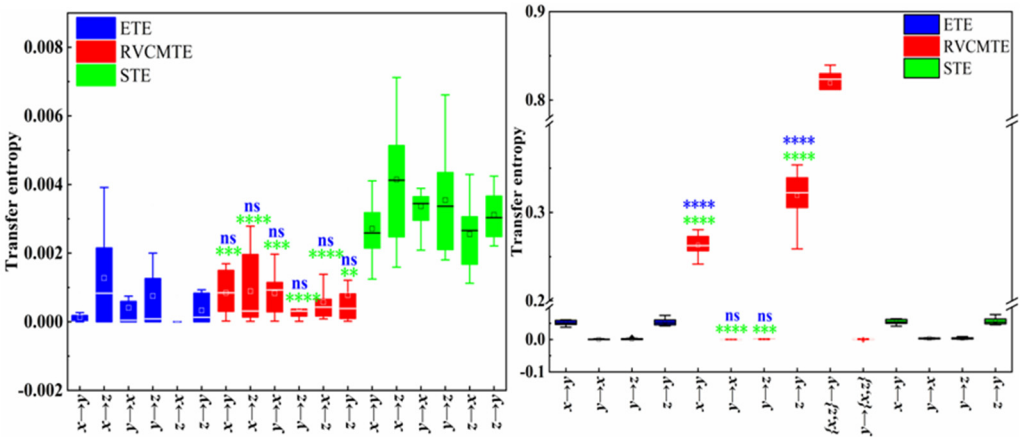

(a) Model I (b) Model II

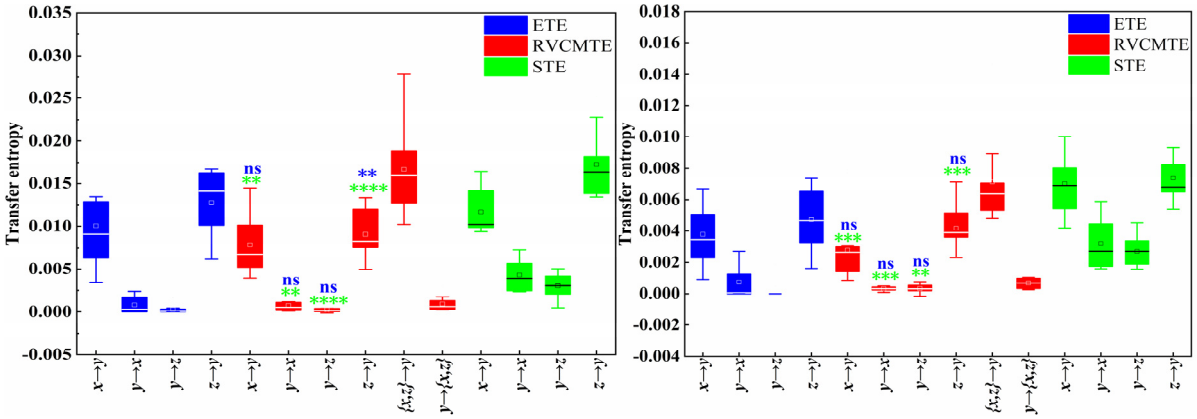

(c) Model III (b) Model IV

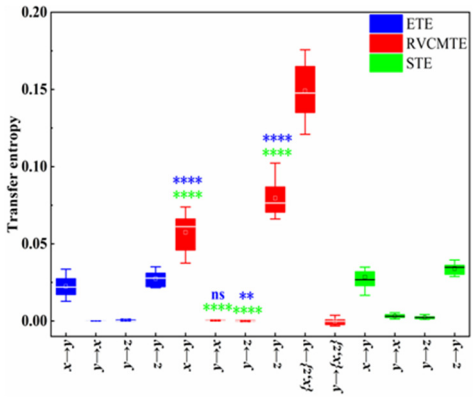

(e) Model V

Figure 1. Performance comparison of different entropy transfer methods. "ns": $P > 0.05$, "*": $P < 0.05$, "**": $P < 0.01$, "***": $P < 0.001$, "****": $P < 0.0001$.

To sum up, since the RVCMTE method utilizes the more flexible R-vine copula function to calculate the transfer entropy value, it can effectively avoid the problem that the joint probability distribution is difficult to estimate compared with traditional transfer entropy algorithms. And compared with other copula estimation methods, it can solve the high-dimensional limitation of variables and avoid the complicated selection of copula functions. In addition, it can be seen from the simulation results that the RVCMTE algorithm is more accurate in calculating the causal relationship between variables.

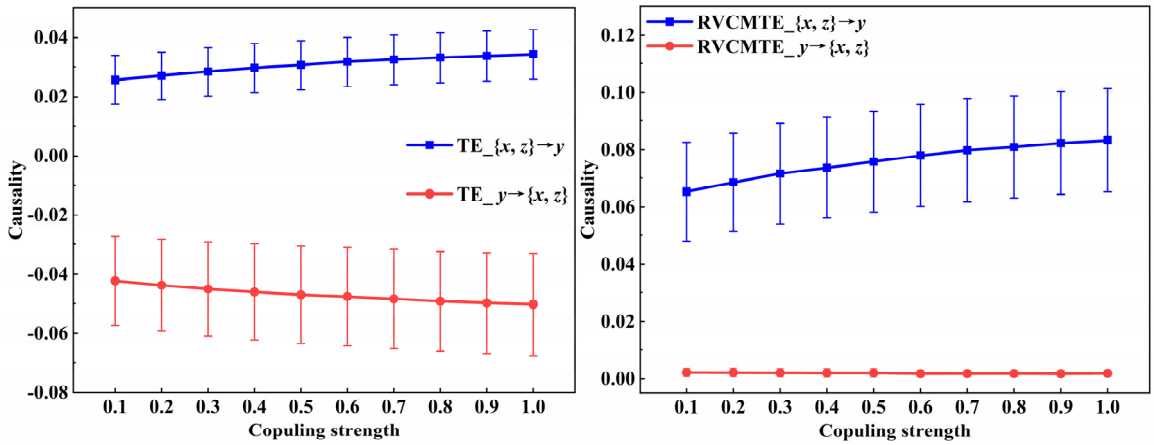

Figure 2. Comparison of GCMTE and RVCMTE estimation results.

To further examine the performance of our method, we systematically varied the sample size and the noise level. Taking model V as an example, the data comprising a different number of samples (500, 1000, 1500 and 2000) are used for test. For a given data length, we generated 10 trials of time series. The RVCMTE causality analysis is performed on individual trials and its statistical significance is tested ($P < 0.05$). As shown in Figure 3(a), as the number of samples increases, the values of y to x, y to z and y to $\{x, z\}$ are all close to zero, which is the same as the theoretical value. However, the values of $\{x, z\}$ to y and z to y are fluctuating, which means that the RVCMTE algorithm is affected by data length. Starting from the number of samples in the experimental setup, the minimum sample size should be controlled ~1500. As shown in Figure 3(b), when the performance of RVCMTE is tested at different noise levels by varying the noise coefficients (0.5, 1, 1.5 and 2), the change of noise coefficient has little effect on the transfer entropy value. We also performed a t-test on the simulation results under different noise levels and found that the RVCMTE algorithm as a whole can still maintain consistent detection results ($P > 0.05$) which demonstrates that RVCMTE is not affected by noise.

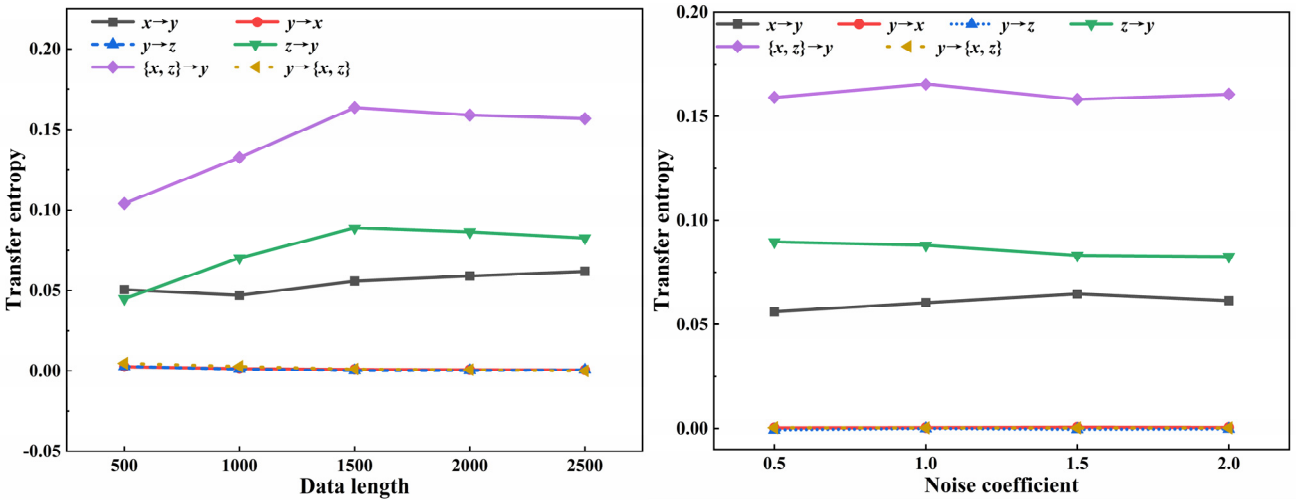

(a) Sample size (b) Noise coefficients

Figure 3. Comparison of RVCMTE results with different sample sizes and noise coefficients.

3.2. Applications to sEMG data

3.2.1. Subjects and experiment paradigm

The data was collected from thirteen participants (all males aged between 21–26 and all of whom were right-handed) after we explained the study to them. All the subjects were informed of the details of the experiments and signed the informed consent form according to the Helsinki Declaration, and all measurements were approved by the Hangzhou Dianzi University's Institutional Review Board. The participants did not drink alcohol, coffee, strong tea, or sports drinks the day before the experiment nor did they smoke or exercise vigorously.

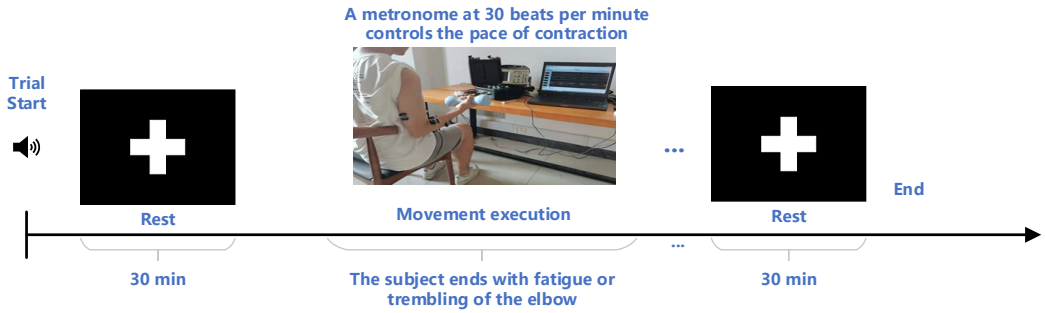

Figure 4. Experiment paradigm.

During the experiments, each subject was asked to sit in an electrically shielded room with their upper arm fixed, and then they were directed to move their lower arm with a 2 kg dumbbell in the sagittal plane at a speed of 20 repetitions per minute by following a metronome. The subjects were requested to continue lifting the dumbbells until they expressed fatigue or experienced trembling of the elbow, after which they rested for 30 minutes and repeated the process, as shown in Figure 4. Each

subject performed five trials. The first 20 seconds and last 20 seconds of the signals are considered as the non-fatigue and fatigue conditions respectively.

3.2.2. Data recording and preprocessing

The skin surface was carefully prepared and cleaned with alcohol before the electrodes were attached. The electrode was placed on the area of greatest muscle bulk along the longitudinal midline of the muscle, which was selected based on the Surface EMG for non-invasive assessment of muscles project. sEMG signals were recorded using the TrignoTM wireless sEMG signal acquisition device produced by Delsys, USA. The sampling frequency was set to 1926 Hz. The experiment collected 6-channel sEMG signals from the right hand, including flexor carpi radialis (FCR), flexor carpi ulnaris (FCU), brachioradialis (BR), triceps brachii (TB), biceps brachii (BB), and extensor digitorum (ED), as shown in Figure 5.

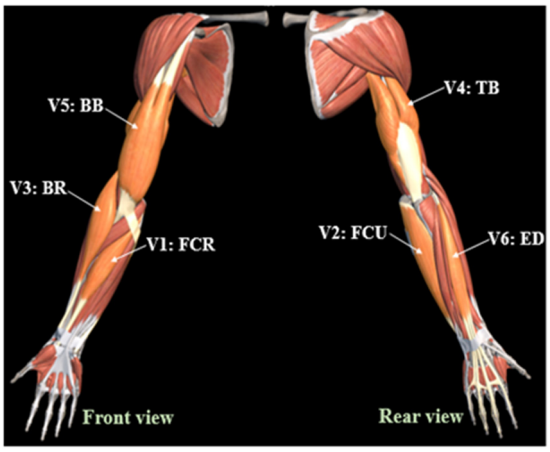

Figure 5. Illustration of EMG electrode placement.

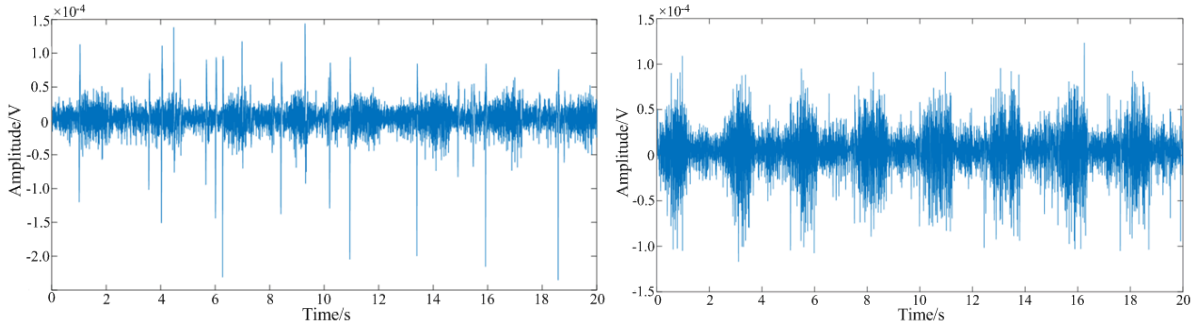

(a) Non-fatigue segments (b) Fatigue segments

Figure 6. Raw sEMG signals.

As sEMG signals are weak and susceptible to high-frequency noise, to obtain more effective sEMG features, it is necessary to preprocess the collected sEMG signals. De-averaging and a high-pass filter were used to remove baseline drift. The infinite impulse response notch filter was used to

remove the 50 Hz power signal, and then the Chebyshev type II band-pass filter was employed to extract the sEMG signals in the 21–60 Hz (beta and gamma) frequency band to construct the intermuscular network [35]. Comparisons of before fatigue and fatigue signals in the time domain and frequency domain are presented in Figures 6 and 7.

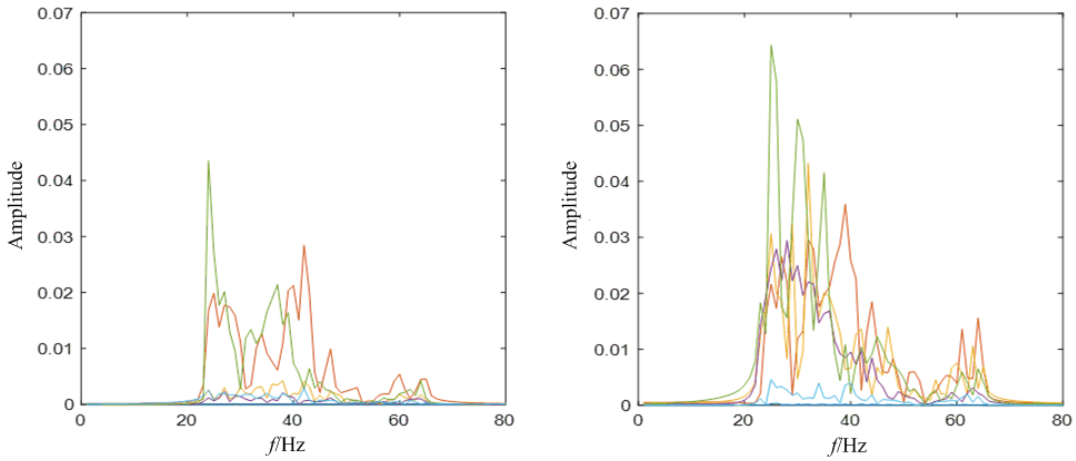

(a) Non-fatigue segments (b) Fatigue segments

Figure 7. Pre-processing of sEMG signals.

During the sEMG signal acquisition experiment, different subjects showed different amplitudes and times to fatigue. These differences depend on the height, weight and muscle mass of the participants. It can be seen from Figures 6 and 7 that compared with the non-fatigue stage, the amplitude of this spectrum is higher and a large number of spikes are found in low frequency region. This can be due to the large number of motor units which are recruited during fatigue. A shift in spectrum towards the low frequency region is observed during the fatigue condition.

In this paper, the integrated electromyography (IEMG) [36], root mean square (RMS) [37], mean power frequency (MPF) [38] and median frequency (MF) [39] of the collected data were calculated to further determine the state of muscle fatigue. As detailed in Tables 1 and 2, the values of IEMG and RMS fatigue show an overall increasing trend compared with non-fatigue, while the MF and MPF values generally exhibited a downward trend, which was consistent with the expected results.

Table 1. Characteristic parameters of sEMG signals before fatigue.

Before	IEMG	RMS	MF	MPF
V1	7.891e-05	1.255e-04	121.517	213.482
V2	6.960e-05	1.720e-04	61.256	173.405
V3	2.957e-05	6.029e-05	112.309	205.648
V4	9.476e-06	1.332e-05	90.284	182.703
V5	9.183e-05	1.278e-04	100.051	191.078
V6	5.992e-05	1.123e-04	73.358	184.322

Table 2. Characteristic parameters of sEMG signals after fatigue.

Before	IEMG	RMS	MF	MPF
V1	1.033e-04	1.637e-04	105.533	195.438
V2	8.559e-05	2.373e-04	76.996	168.777
V3	3.405e-05	5.220e-05	120.125	212.556
V4	2.721e-05	6.956e-05	76.094	177.773
V5	1.306e-04	1.835e-04	90.960	189.187
V6	4.936e-05	8.415e-05	80.556	176.173

3.2.3. Construction of intermuscular coupling network using RVCMTE

An $N \times N$ binary graph muscle network consisting of nodes (muscles) and directed edges (connectivity) between the nodes was constructed by applying a threshold to the connection matrix calculated by RVCMTE. Here, N is set to be 6 because there are 6 EMG electrodes in our experiment. We use the nonparametric kernel estimation method, select the Gaussian kernel function, and determine the bandwidth according to the empirical rule $h \approx 1.06\hat{\sigma}^{-0.5}$, where $\hat{\sigma}$ is the standard deviation of x_i. We calculate the RVCMTE and then take the average RVCMTE of all subjects. To satisfy the algebraic connectivity of the network as much as possible, the node degree must be at least greater than 1. The binary matrix is performed by setting the 1%*max (RVCMTE) value to the equal interval threshold [40]. Furthermore, the igraph package is used to draw the intermuscular coupling network, and the best community structure of the intermuscular coupling network is obtained according to the maximum modularity score. The average results obtained by all subjects are shown in Figure 8, where the nodes under the same color are in a community and the direction of the arrow represents the flow of causal information between muscles.

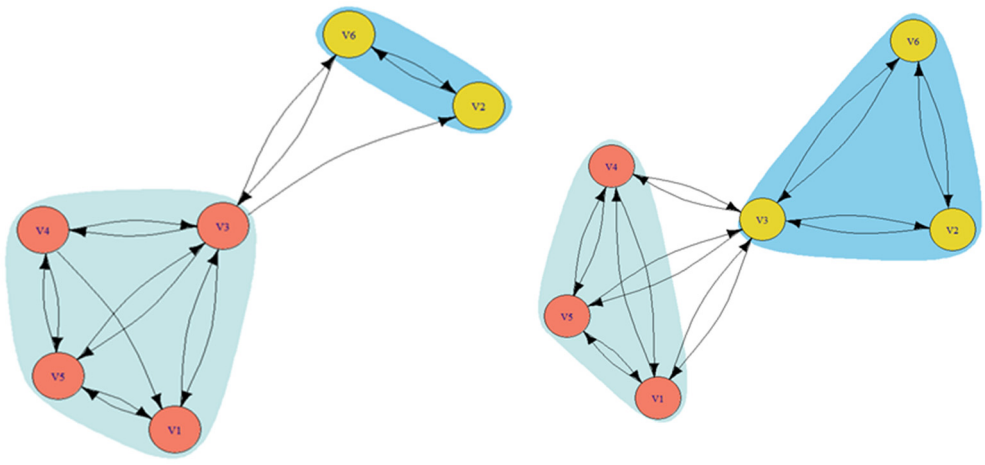

(a) Non-fatigue (b) Fatigue

Figure 8. Intermuscular coupling networks in non-fatigue and fatigue states.

As shown in Figure 8, both the non-fatigue segment and the fatigue segment are divided into two community structures, which reflect the self-organization function of each muscle node. V3 acts as a

bridge between the two communities, enjoying extensive two-way connections. In Figure 8(a), the communities composed of V2 (FCU) and V6 (ED) are also closer in actual muscle positions. The one-way connection between V4 (TB) and V1 (FCR), and the one-way connection between V3 (BR) and V2 (FCU) means when performing a bicep curl, the upper arm has a greater influence on the information transmission of the lower arm. With muscle fatigue, the community structure changes, V3 undergoes community transfer, and the one-way connection of V4 (TB) to V1 (FCR), V3 (BR) to V2 (FCU) has also changed into a two-way connection. This reflects that in the fatigue state, to control the muscle group to continue to complete the required action, the coupling relationship between the communities is changed. The information transmission between muscles is also bidirectional at the upper and lower ends of the physical position and this is more obvious when the muscles are fatigued.

3.2.4. Intermuscular coupling network analysis

1) Network parameters

Next, six complex network topological parameters: degree, clustering coefficient, average distance, density, reciprocity [41] and modularity [35] are employed to explore the characteristics of different states of muscles from the perspective of the intermuscular network. The topological parameters of the coupled network in the non-fatigue state and the fatigue state are obtained as shown in Figure 9.

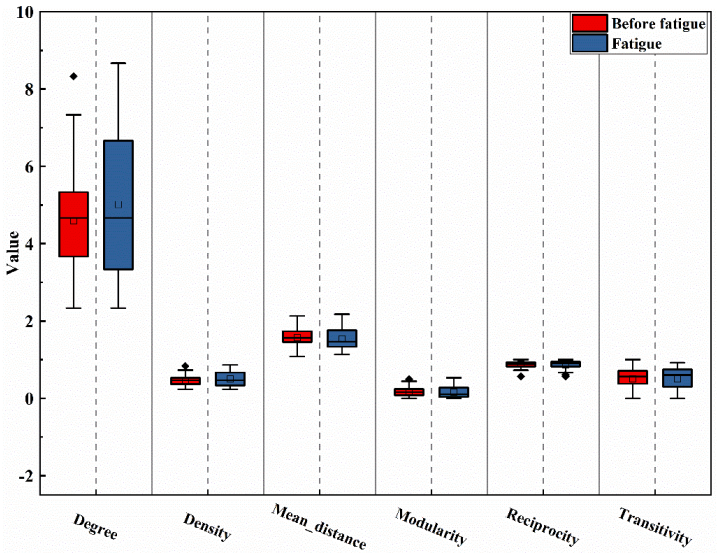

Figure 9. Topological parameters of the coupled network in non-fatigue and fatigue states.

As shown in Figure 9, the network parameters corresponding to the intermuscular coupling network in a non-fatigue and fatigue state show a consistent distribution rule ($P > 0.05$). Only the value of degree after fatigue increases slightly. After the muscle enters the fatigue state, to maintain continuous movement, more motor neurons will participate in the information interaction, resulting in an increase in the interaction degree between nodes [42]. It is not difficult to find that the change of the coupling relationship of muscle groups depends on the production of a specific action. It has a limited effect on the intermuscular coupling relationship under the same movement.

2) Community causal coupling analysis

Finally, to further explore the differences in casual coupling between the non-fatigue and fatigue state, we use the advantages of RVCMTE multivariate simultaneous analysis to quantitatively measure the strength of the causal coupling between communities shown in Figure 9. The results obtained (mean ± standard deviation) are shown in Figure 10. The t-test result is above the error bar graph. C1 includes nodes V2 and V6, and C2 includes nodes V1, V3, V4, and V5. C3 includes nodes V2, V3, and V6, and C4 includes V1, V4, and V5.

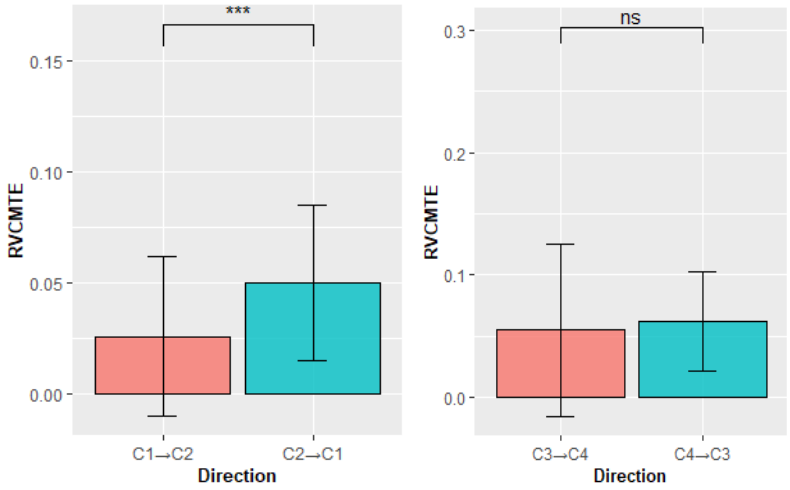

(a) Non-fatigue (b) Fatigue

Figure 10. Comparison of the coupling strength between different communities.

As shown in Figure 10(a), the causal coupling strength of C2 to C1 is significantly higher than that of C1 to C2 ($P < 0.05$). From the intermuscular coupling network (Figure 8(a)), it can also be found that C2 includes more nodes and its own coupling network is also more complex. C2 (V3) points to the one-way channel of C1 (V2), so C2 more clearly exhibits a causal drive to C1. As shown in Figure 10(b), there is no significant difference in the mutual coupling strength between C3 and C4 ($P > 0.05$). The results show that 1) there is a certain difference in the causal coupling strength between communities before fatigue, the two-way coupling between communities is not sufficient. After entering a state of fatigue, in order to complete the action, the node interaction is fully mobilized so that the information flow between each community structure realizes two-way circulation; and 2) when the muscle tissue cooperates to complete the action, the neuromuscular system is a multiple network of parallel and hierarchical control [43], fatigue will cause the adjustment of the inner network structure, and the causal driving relationship between the hierarchical communities is similar.

4. Discussion

For research on the causality between variables, RVCETE is proposed, benefitting from R-vine copula's unique advantages in multivariate correlation modeling and the powerful linear and non-linear causal analysis capabilities of transfer entropy. Different from traditional kernel estimation methods,

RVCMTE removes the strict requirements for high-dimensional joint probability density functions. In addition, this method does not make a priori assumptions about the distribution type of variables. At the same time, a completely different dependency structure between variables is allowed, which is more flexible and changeable. The simulation results show that compared to the transfer entropy methods (STE and ETE), RVCMTE performs well on various types of simulation data. Not only is the scope of application wider, but the estimation results are more convincing (Figure 1). Compared with Gaussian copula's multivariable transfer entropy, RVCMTE is more sensitive and robust to the dynamic changes of causal coupling strength (Figure 1(e)). This may be because the Gaussian copula function is only suitable for symmetrical and asymptotically independent tails, and it is difficult to fit the upper and lower tail-related structures of variables [44]. The R-vine copula function based on the hybrid pairwise copula decomposition achieves good data adaptation performance and the likelihood level is higher [45].

In this paper, binary and multivariate forms of R-vine copula multivariate transfer entropy are used to study the causal coupling between muscles and communities in a non-fatigue and fatigue state. To obtain a clearer community topology, we used 21–60 Hz multi-channel sEMG data. The experiment results show that there are two stable community structures formed between the non-fatigued and fatigued muscles. However, there is a clear difference in the coupling strength between the two communities in the non-fatigue state, where C2 contains more muscle nodes and the internal coupling effect is stronger. Furthermore, there is a one-way causal drive between C2 and C1, which proves that before the muscle enters a state of fatigue, there is often one or several key communities that play a leading role and the causal connection between community structures and nodes within the community are reflected in certain key nodes, such as V3 (BR). This may be related to the need to coordinate and integrate many muscles in the central nervous system during daily movement. If the muscle system which is composed of thousands of motor units is directly controlled, this will inevitably inflict a huge computational burden on the central nervous system. Muscle synergy theory also suggests that the central nervous system does not innervate each muscle individually, but reduces a redundant degree of freedom in human motor control by combining a small number of muscle synergistic units in different ways [46].

Boonstra et al. [43] clarified that the neuromuscular system is a multiple network that allows parallel and hierarchical control based on complex network theory. A muscle can be part of multiple muscle networks, a network can activate multiple muscles, and the intermuscular coupling networks on different frequency bands show different strengths of functional connectivity. After entering the fatigue state, it can be found that the community structure is adjusted, and the community relations with significant differences are transformed into structures with similar coupling strength. In the fatigue state, it is difficult to support the execution requirements by relying mainly on the key community or key node. Each muscle node is fully activated, so that the relevant muscle tissues can play their role, and then the community structure is adjusted to a balanced direction, the information interaction between each muscle and each community is strengthened, and the average degree is improved (Figure 9). There is no significant difference in the network parameters, which should be related to the same action [47].

To sum up, RVCMTE is simple in principle and achieves improved performance compared with traditional methods. However, this research has some shortcomings. Although the R-vine copula function is not limited by the dimension through selecting and combining different pairs of copula, the time cost required to determine the best R-vine matrix is extremely large, which needs further saving

and optimization.

5. Conclusions

In this paper, a novel method of RVCMTE is proposed for coupling analysis, which uses the R-vine copula function to estimate the multivariate transfer entropy. A series of simulations were performed to demonstrate its effectiveness. Compared with traditional TE methods, the RVCMTE is more accurate when judging various complicated causal relationships among variables. Furthermore, the RVCMTE is applied to the analysis of the intermuscular coupling network during non-fatigue and fatigue states. Experimental results show that the coupling relationship between the muscles will gradually deepen when the muscle group enters a fatigue state. It is an effective causal coupling analysis method that provides a new perspective for exploring the control and response mechanisms of human motor functions.

Acknowledgments

This work was supported by National Natural Science Foundation of China under Grant (No. 61871427) and Zhejiang Provincial Natural Science Foundation of China under Grant (No. LZ22F010003).

Conflict of interest

The authors declare there is no conflict of interest.

References

1. M. Bourguignon, V. Jousmaki, S. S. Dalai, K. Jerbi, X. D. Tiège, Coupling between human brain activity and body movements: Insights from non-invasive electromagnetic recordings, *Neuroimage*, **203** (2019), 116177. https://doi.org/10.1016/j.neuroimage.2019.116177
2. Q. She, H. Zheng, T. Tan, B. Zhang, Y. Fan, Z. Luo, Time-frequency-domain copula-based Granger causality and application to corticomuscular coupling in stroke, *Int. J. Human. Robot.*, **16** (2019), 1950018. https://doi.org/10.1142/S021984361950018X
3. P. Grosse, M. J. Cassidy, P. Brown, EEG-EMG, MEG-EMG and EMG-EMG frequency analysis: physiological principles and clinical applications, *Clin. Neurophysiol.*, **113** (2002), 1523–1531. https://doi.org/10.1016/S1388-2457(02)00223-7
4. X. Chen, P. Xie, Y. Zhang, Y. Chen, S. Cheng, L. Zhang, Abnormal functional corticomuscular coupling after stroke, *Neuroimage-Clinical*, **19** (2018), 147–159. https://doi.org/10.1016/j.nicl.2018.04.004
5. C. M. Laine, F. J. Valero-Cuevas, Parkinson's disease exhibits amplified intermuscular coherence during dynamic voluntary action, *Front. Neurol.*, **11** (2020), 204. https://doi.org/10.3389/fneur.2020.00204
6. E. Colamarino, V. D. Seta, M. Masciullo, F. Cincotti, D. Mattia, F. Pichiorri, et al., Corticomuscular and intermuscular coupling in simple hand movements to enable a hybrid brain-computer interface, *Int. J. Neural Syst.*, **31** (2021), 2150052. https://doi.org/10.1142/s0129065721500520

7. V. Medved, S. Medved, I. Kovač, Critical appraisal of surface electromyography (sEMG) as a taught subject and clinical tool in medicine and kinesiology, *Front. Neurol.*, **11** (2020), 1–17. https://doi.org/10.3389/fneur.2020.560363
8. C. J. Houtman, D. F. Stegeman, J. P. V. Dijk, M. J. Zwarts, Changes in muscle fiber conduction velocity indicate recruitment of distinct motor unit populations, *J. Appl. Physiol.*, **95** (2003), 1045–1054. https://doi.org/10.1152/japplphysiol.00665.2002
9. J. Murillo-Escobar, Y. E. Jaramillo-Munera, D. A. Orrego-Metaute, E. Delgado-Trejos, D. Cuesta-Frau, Muscle fatigue analysis during dynamic contractions based on biomechanical features and permutation entropy, *Math. Biosci. Eng.*, **17** (2020), 2592–2615. https://doi.org/10.3934/mbe.2020142
10. S. E. Jero, K. D. Bharathi, P. A. Karthick, S. Ramakrishnan, Muscle fatigue analysis in isometric contractions using geometric features of surface electromyography signals, *Biomed. Signal. Process.*, **68** (2021), 1–11. https://doi.org/10.1016/j.bspc.2021.102603
11. Q. Gao, J. Liu, Z. Ju, X. Zhang, Dual-hand detection for human-robot interaction by a parallel network based on hand detection and body pose estimation, *IEEE Trans. Ind. Electron.*, **66** (2019), 9663–9672. https://doi.org/10.1109/TIE.2019.2898624
12. Q. Gao, J. Liu, Z. Ju, Robust real-time hand detection and localization for space human robot interaction based on deep learning, *Neurocomputing*, **390** (2020), 198–206. https://doi.org/10.1016/j.neucom.2019.02.066
13. Y. Sun, C. Xu, G. Li, F. Wan, J. Kong, D. Jiang, et al., Intelligent human computer interaction based on non redundant EMG signal, *Alex. Eng. J.*, **59** (2020), 1149–1157. https://doi.org/10.1016/j.aej.2020.01.015
14. Z. Yang, D. Jiang, Y. Sun, B. Tao, X. Tong, G. Jiang, et al., Dynamic gesture recognition using surface EMG signals based on multi-stream residual network, *Front. Bioeng. Biotechnol.*, **9** (2021), 779353. https://doi.org/10.3389/fbioe.2021.779353
15. J. Qi, G. Jiang, G. Li, Y. Sun, B. Tao, Surface EMG hand gesture recognition system based on PCA and GRNN, *Neural. Comput. Appl.*, **32** (2020), 6343–6351. https://doi.org/10.1007/s00521-019-04142-8
16. Y. Cheng, G. Li, M. Yu, D. Jiang, J. Yun, Y. Liu, et al., Gesture recognition based on surface electromyography-feature image, *Concurr. Comput. Pract. Exp.*, **33** (2021), e6051. https://doi.org/10.1002/cpe.6051
17. R. Ma, L. Zhang, G. Li, D. Jiang, S. Xu, D. Chen, Grasping force prediction based on sEMG signals, *Alex. Eng. J.*, **59** (2020), 1135–1147. https://doi.org/10.1016/j.aej.2020.01.007
18. O. Sporns, Graph theory methods: Applications in brain networks, *Dialogues Clin. Neurosci.*, **20** (2018), 111–120. https://doi.org/10.31887/dcns.2018.20.2/osporns
19. J. N. Kerkman, D. Andreas, L. L. Gollo, B. Michael, T. W. Boonstra, Network structure of the human musculoskeletal system shapes neural interactions on multiple timescales, *Sci. Adv.*, **4** (2018), 0497. https://doi.org/10.1126/sciadv.aat0497
20. T. W. Boonstra, L. Faes, J. N. Kerkman, D. Marinazzo, Information decomposition of multichannel EMG to map functional interactions in the distributed motor system, *Neuroimage*, **202** (2019), 116093. https://doi.org/10.1016/j.neuroimage.2019.116093
21. L. Barnett, A. K. Seth, The MVGC multivariate Granger causality toolbox: A new approach to Granger-causal inference, *J. Neurosci. Methods*, **223** (2014), 50–68. https://doi.org/10.1016/j.jneumeth.2013.10.018

22. P. A. Stokes, P. L. Purdon, A study of problems encountered in Granger causality analysis from a neuroscience perspective, in *Proceedings of the National Academy of Sciences*, **114** (2017), 7063–7072. https://doi.org/10.1073/pnas.1704663114
23. T. Schreiber, Measuring information transfer, *Phys. Rev. Lett.*, **85** (2000), 461–464. https://doi.org/10.1103/physrevlett.85.461
24. R. Marschinski, H. Kantz, Analysing the information flow between financial time series, *Eur. Phys. J. B.*, **30** (2002), 275–281. http://dx.doi.org/10.1140/epjb/e2002-00379-2
25. H. Kiwata, Analysis of dynamic Ising model by a variational approximate method: Estimation of transfer entropy, *Phys. Rev. E.*, **101** (2020), 042102. https://doi.org/10.1103/PhysRevE.101.042102
26. A. Sklar, Random variables, joint distributions, and copulas, *Kybernetica*, **9** (1973), 449–460.
27. S. R. Kasa, S. Bhattacharya, V. Rajan, Gaussian mixture copulas for high-dimensional clustering and dependency-based subtyping, *Bioinformatics*, **36** (2020), 621–628. https://doi.org/10.1093/bioinformatics/btz599
28. T. M. Erhardt, C. Czado, U. Schepsmeier, R-vine models for spatial time series with an application to daily mean temperature, *Biometrics*, **71** (2015), 323–332. http://dx.doi.org/10.1111/biom.12279
29. M. Hu, H. Liang, A copula approach to assessing Granger causality, *Neuroimage*, **100** (2014), 125–134. https://doi.org/10.1016/j.neuroimage.2014.06.013
30. F. Sun, W. Zhang, N. Wang, W. Zhang, A copula entropy approach to dependence measurement for multiple degradation processes, *Entropy*, **21** (2019), 724. https://doi.org/10.3390/e21080724
31. U. Schepsmeier, A goodness-of-fit test for regular vine copula models, *Econ. Rev.*, **38** (2019), 25–46. http://dx.doi.org/10.1080/07474938.2016.1222231
32. J. Dissmann, E. C. Brechmann, C. Czado, D. Kurowicka, Selecting and estimating regular vine copula and application to financial returns, *Comput. Stat. Data Anal.*, **59** (2013), 52–69. http://dx.doi.org/10.1016/j.csda.2012.08.010
33. J. Ma, Discovering association with copula entropy, preprint, arXiv:1907.12268, 2019. https://arxiv.org/abs/1907.12268
34. T. Bedford, R. M. Cooke, Probability density decomposition for conditionally dependent random variables modeled by vines, *Ann. Math. Artif. Intell.*, **32** (2001), 245–268. http://dx.doi.org/10.1023/A:1016725902970
35. J. N. Kerkman, A. Bekius, T. W. Boonstra, A. Daffertshofer, N. Dominic, Muscle synergies and coherence networks reflect different modes of coordination during walking, *Front. Physiol.*, 11 (2020), 751. https://doi.org/10.3389/fphys.2020.00751
36. S. Wang, J. Zheng, B. Zheng, X. Jiang, Phase-based grasp classification for prosthetic hand control using sEMG, *Biosensors*, **12** (2022), 57. https://doi.org/10.3390/bios12020057
37. D. Chmielewska, G. Sobota, P. Dolibog, P. Dolibog, A. Opala-Berdzik, Reliability of pelvic floor muscle surface electromyography (sEMG) recordings during synchronous whole body vibration, *Plos One*, **16** (2021), e0251265. https://doi.org/10.1371/journal.pone.0251265
38. C. Wang, M. Cai, Z. Hao, S. Nie, C. Liu, H. Du, et al., Stretchable, multifunctional epidermal sensor patch for surface electromyography and strain measurements, *Adv. Intell. Syst.*, **3** (2021), 2100031. http://dx.doi.org/10.1002/aisy.202100031
39. J. D. Cavalcanti, G. A. F. Fregonezi, A. J. Sarmento, T. Bezerra, L. P. Gualdi, F. Pennati, et al., Electrical activity and fatigue of respiratory and locomotor muscles in obstructive respiratory diseases during field walking test, *Plos One*, **17** (2022), e0266365. https://doi.org/10.1371/journal.pone.0266365

40. J. G. Augustson, J. Minker, An analysis of some graph theoretical cluster techniques, *J. ACM.*, **17** (1970), 571–588. https://doi.org/10.1145/321607.321608
41. M. Windzio, The "social brain" reciprocity, and social network segregation along ethnic boundaries, *Hum. Nat.*, **31** (2020), 443–461. https://doi.org/10.1007/s12110-020-09382-5
42. J. Ushiyama, M. Katsu, Y. Masakado, A. Kimura, M. Liu, J. Ushiba, Muscle fatigue-induced enhancement of corticomuscular coherence following sustained submaximal isometric contraction of the tibialis anterior muscle, *J. Appl. Physiol.*, **110** (2011), 1233–1240. https://doi.org/10.1152/japplphysiol.01194.2010
43. T. W. Boonstra, A. Danna-Dos-Santos, H. B. Xie, M. Roerdink, J. F. Stins, M. Breakspear, Muscle networks: Connectivity analysis of EMG activity during postural control, *Sci. Rep.*, **5** (2015), 1–14. https://doi.org/10.1038/srep17830
44. A. Zhang, J. Fang, W. Hu, V. D. Calhoun, Y. Wang, A latent Gaussian copula model for mixed data analysis in brain imaging genetics, *IEEE/ACM Trans. Comput. Biol. Bioinform.*, **18** (2021), 1350–1360. https://doi.org/10.1109/TCBB.2019.2950904
45. M. T. Amin, F. Khan, S. Ahmed, S. Imtiaz, Risk-based fault detection and diagnosis for nonlinear and non-Gaussian process systems using R-vine copula, *Process Saf. Environ. Prot.*, **150** (2021), 123–136. https://doi.org/10.1016/j.psep.2021.04.010
46. K. M. Steele, M. C. Tresch, E. J. Perreault, The number and choice of muscles impact the results of muscle synergy analyses, *Front. Comput. Neurosci.*, **7** (2013), 105. http://dx.doi.org/10.3389/fncom.2013.00105
47. C. Li, G. Li, G. Jiang, D. Chen, H. Liu, Surface EMG data aggregation processing for intelligent prosthetic action recognition, *Neural Comput. Appl.*, **32** (2020), 16795–16806. https://doi.org/10.1007/s00521-018-3909-z